Velocity-dependent transverse momentum distribution of fragments produced from ^{40}Ar+ ^{9}Be at 95 MeV/nucleon

S. Momota,[1] I. Tanihata,[2] A. Ozawa,[3] M. Notani,[4] K. Yoshida,[5] K. Morimoto,[5] T. Yamaguchi,[6] T. Onishi,[7] A. Yoshida,[5] Y. X. Watanabe,[8] Z. Liu,[9] and A. Ono[10]

[1]*Kochi University of Technology, Kochi 782-8502, Japan*
[2]*RCNP, Osaka University, Mihogaoka, Ibaraki, Osaka 567-0047, Japan*
[3]*Institute of Physics, University of Tsukuba, Ibaraki 305-8571, Japan*
[4]*The Enrico Fermi Institute, University of Chicago, Chicago, Illinois 60637, USA*
[5]*RIKEN, 2-1 Hirosawa, Wako, Saitama, Japan*
[6]*Department of Physics, Saitama University, Saitama 338-8570, Japan*
[7]*Hitachi High-Technologies Co., Oaza, Ichige, Hitachinaka, Ibaraki 312-8504, Japan*
[8]*High Energy Accelerator Research Organization (KEK), Ibaraki 305-0801, Japan*
[9]*Institute of Modern Physics, Chinese Academy of Sciences, Lanzhou 730000, China*
[10]*Department of Physics, Tohoku University, Sendai 980-8578, Japan*

(Received 8 May 2015; published 10 August 2015)

Transverse momentum (P_T) distributions of projectilelike fragments produced at intermediate energy are investigated. P_T distributions of fragments with mass A_F = 10–37, produced from an ^{40}Ar beam with E = 95 MeV/nucleon and a Be target, are observed as a function of fragment velocity by using the Rikagaku Kenkyusho (RIKEN) Projectile Fragment Separator at RIKEN. The width of P_T distribution (σ_T) decreases monotonically with longitudinal momentum (P_L). The decreasing trend shows a clear dependence on fragment mass. The observed σ_T is analyzed with a linear function and successfully reproduced by a parameter to characterize the decreasing trend. σ_T at the primary beam velocity shows good agreement with the Goldhaber formula, which is obtained on the basis of the contribution of the Fermi momentum. In contrast, the σ_T at the center of the P_L distribution as determined by using the fits and parametrized energy loss in the fragmentation process is consistent with the width, which includes an additional contribution from the orbital deflection of the projectile. The antisymmetrized molecular-dynamics calculation indicates that the contribution of impact parameters is an important factor in understanding the behavior of the P_T distribution. In addition, the practical formulation for σ_T obtained in the present study enables a reliable characterization of the fragments, which would be applicable to various research fields involving, for example, radioactive nuclear beams.

DOI: 10.1103/PhysRevC.92.024608 PACS number(s): 25.70.Mn, 25.60.Gc, 27.20.+n, 27.30.+t

I. INTRODUCTION

The fragmentation process is a powerful method for preparing a wide range of isotopes as secondary beams. The momentum distribution of the reaction products is one of the fundamental parameters whereby a reaction mechanism can be investigated. A series of experimental and theoretical studies on the momentum distribution has been carried out. In addition, radioactive nuclear beams (RNBs), produced from the fragmentation process, have been successfully employed to investigate unique features of exotic nuclei, far from the valley of β stability. The momentum distribution of a fragment is a major factor determining the intensity and purity of RNBs. Therefore, it is very important to determine the systematic behavior of the momentum distributions of fragments in order to be able to perform experiments in which RNBs are used. To evaluate the intensity and quality of RNBs produced through the fragmentation process, a parametrized formulation of the momentum distributions is incorporated using a program, such as LISE++ [1] or MOCADI [2].

At relativistic energies, the fragment momentum distribution shows an isotropic Gaussian shape [3], and the width can be successfully reproduced on the basis of the contribution of the Fermi momentum of nucleons in the fragmentation process as proposed by Goldhaber [4]. At lower energies, the observed momentum distributions have shown deviations from the isotropic shape observed at higher energies. Concerning the longitudinal momentum (P_L), the large number of measurements have been conducted and revealed its systematic behavior. The width of the P_L distribution (σ_L) at higher momentum is represented using the formulation proposed by Goldhaber. In contrast, a tail component or an additional width was observed at lower momentum [5–7]. This behavior is indicative of additional reaction processes, which indicate the collective nature to cause an energy dissipation effect [6]. The behaviors of P_L distributions were formulated by universal parametrization [8] and incorporated into LISE++ [1]. On the other hand, few systematic measurements have been performed for the transverse momentum (P_T) distributions of fragments. At E = 100–250 MeV/nucleon, the width of the P_T distribution (σ_T) has been found to be significantly larger than that of the P_L distribution and the width estimated by the Goldhaber model [9–11]. The additional width of the P_T distribution was empirically formulated on the basis of the width due to orbital deflection arising from nuclear and Coulomb forces of the target nucleus [9,12] in addition to the Goldhaber model. Considering the contributions of the other reaction processes observed in the P_L distribution, the

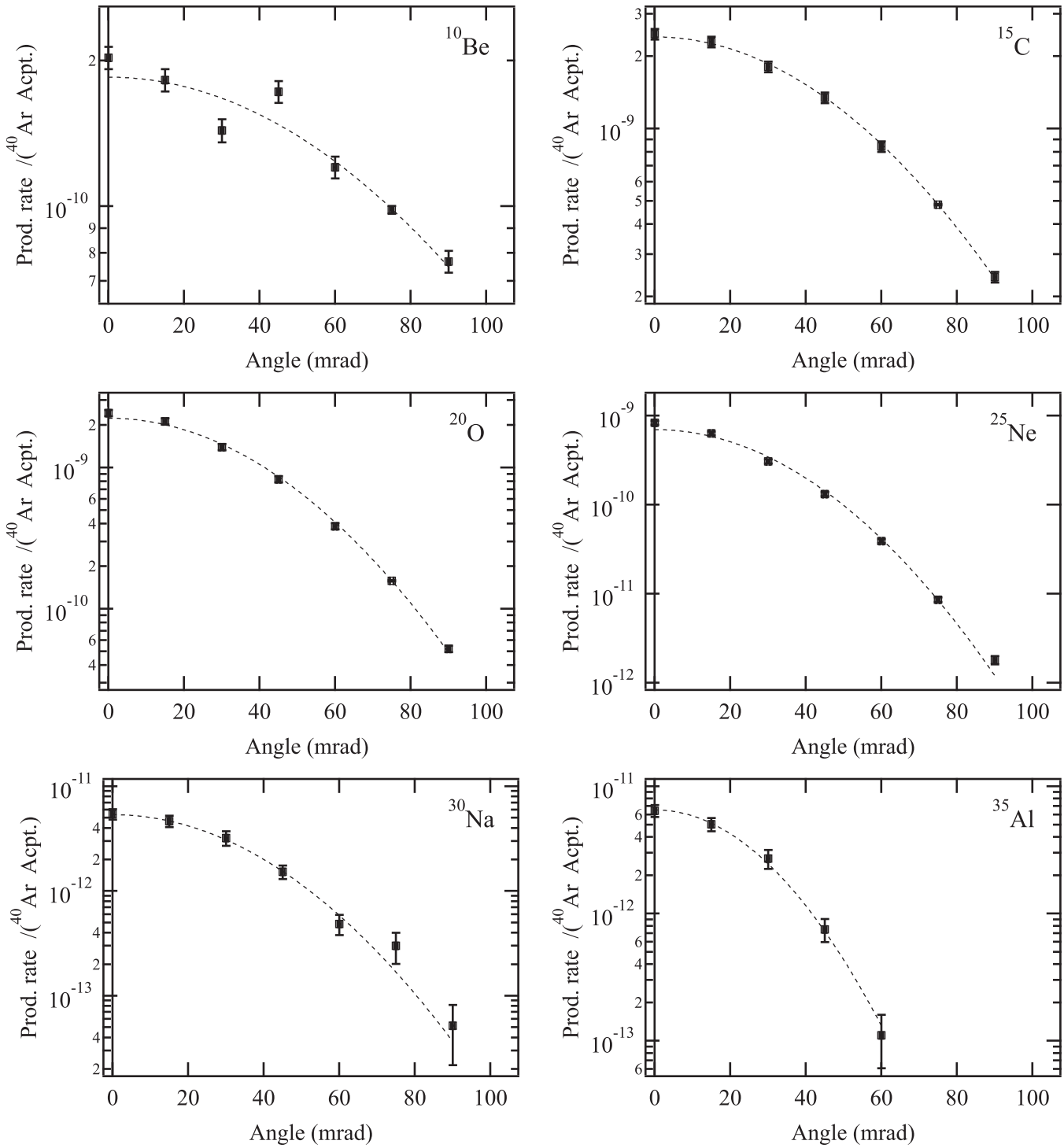

FIG. 1. Angular distributions for fragments observed at $B\rho = 3.60\,\mathrm{Tm}$. Production rate is normalized by the primary beam and the acceptance of the RIPS spectrometer. Dotted lines show the result of fitting with a Gaussian function.

P_T distribution of fragments would have velocity dependence. This additional effect on σ_T was partially observed to be an evolution of angular distribution as a function of fragment velocity at 44 MeV/nucleon [6]. Our previous article [13] reported a clear correlation between σ_T and fragment velocity at 95 MeV/nucleon. However, our description of this correlation was brief, and our quantitative results are insufficient to formulate the σ_T observed in the article.

In the present article, to further investigate the P_T distribution of fragments that were produced at an incident energy of 95 MeV/nucleon, a quantitative analysis is performed on the observed σ_T. The details of the procedures used to obtain

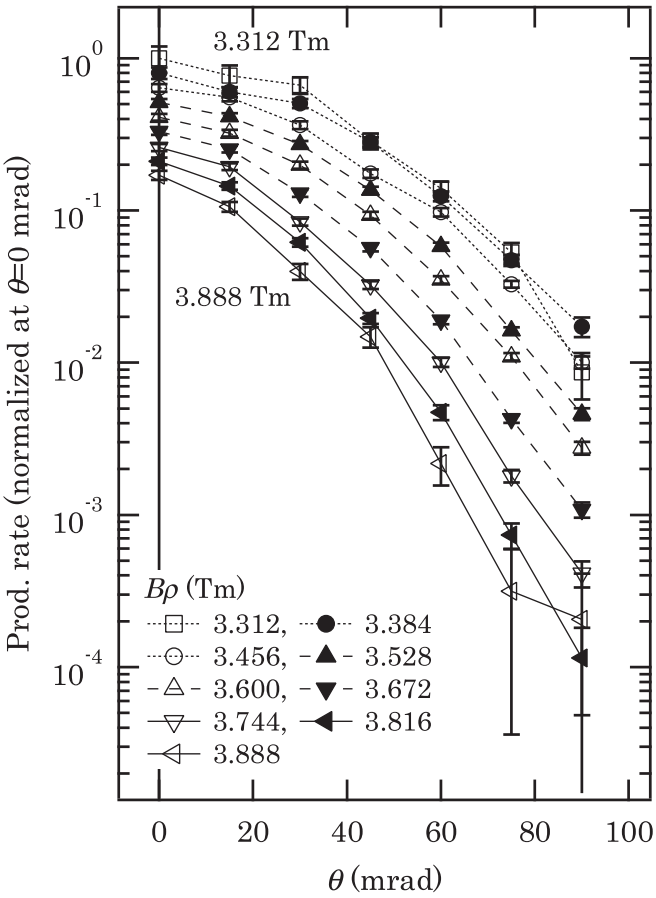

FIG. 2. Evolution of angular distribution of ^{26}Ne observed at $B\rho = 3.312$–3.888 Tm. Production rate is normalized at $\theta = 0$ mrad. Because of the large error due to poor statistics, angular distributions observed at $B\rho = 3.240$ and 3.960 Tm are not shown. The distribution for each $B\rho$ is vertically displaced to make clear the systematic trend.

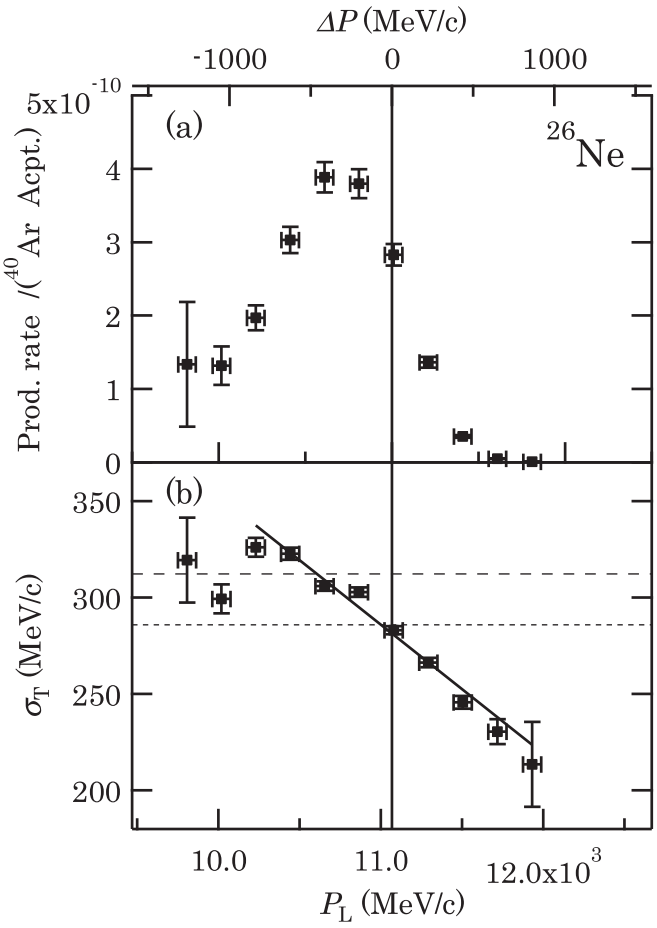

FIG. 3. (a) $P_{\rm L}$ distribution at $\theta_x = 0$ mrad and (b) width of $P_{\rm T}$ distribution ($\sigma_{\rm T}$) for ^{26}Ne. Production rate is normalized by the primary beam and the acceptance of the RIPS spectrometer. The horizontal error bars indicate the momentum acceptance determined by the RIPS separator. The top axis indicates the shift in $P_{\rm L}$ relative to that corresponding to the velocity of projectile (^{40}Ar) at the center position of the Be target. The dotted line and broken line, respectively, indicate the widths of $P_{\rm L}$ distribution $\sigma_{\rm GH}$ and $\sigma_{\rm D}$ defined in the text. $\sigma_0 = 93.5$ MeV/c [7], and $\sigma_1 = 195$ MeV/c are employed for calculation. The solid line in (b) represents the results of fitting with a linear function.

$\sigma_{\rm T}$ from the observed angular distribution and to calculate the errors, which were not described in our previous article, are also described. An antisymmetrized molecular-dynamics (AMD) calculation is performed, and the calculated results are compared with the observed results to understand the behavior of the observed $\sigma_{\rm T}$. The present study will help to elucidate the fragmentation process at $E \approx 100$ MeV/nucleon.

II. EXPERIMENT

The experiment was performed at the Rikagaku Kenkyusho (RIKEN) Accelerator Research Facility. An ^{40}Ar beam, accelerated by the ring cyclotron up to 95 MeV/nucleon, was used to irradiate a 0.5-mm-thick Be target. The energy and its straggling of the incident beams after passing the Be target, which are calculated by ATIMA [14], were 90.23 and 0.04 MeV/nucleon, respectively. In order to identify the reaction products, the projectile fragment separator, RIKEN Projectile Fragment Separator (RIPS) [15], was employed as a doubly achromatic spectrometer. Reaction products were collected and transported to a doubly achromatic focal plane F2. The momentum acceptance of RIPS $\Delta P/P = \pm 0.5\%$ was determined by a pair of slits placed at the momentum dispersive focusing point F1. The angular acceptance ± 7.5 mrad for θ_x and θ_y was defined by a square window formed by four slits (upper, lower, left, and right) located behind the Be target. A pair of swinger magnets, installed upstream of the Be target, was employed to observe the reaction products, which were emitted at angles of $\theta_x \neq 0$ mrad. By exploiting the consecutive deflection effect of the primary beam due to the swinger magnets, the production rates of the fragments produced were monitored over a wide range of θ_x from 0 to 90 mrad, which is larger than the angular acceptance of RIPS. In order to observe the angular distribution, the magnetic-field setting of the swinger magnets was varied in increments of 15 mrad. At each setting, the primary beam position was adjusted to the geometric beam axis by using a fluorescent

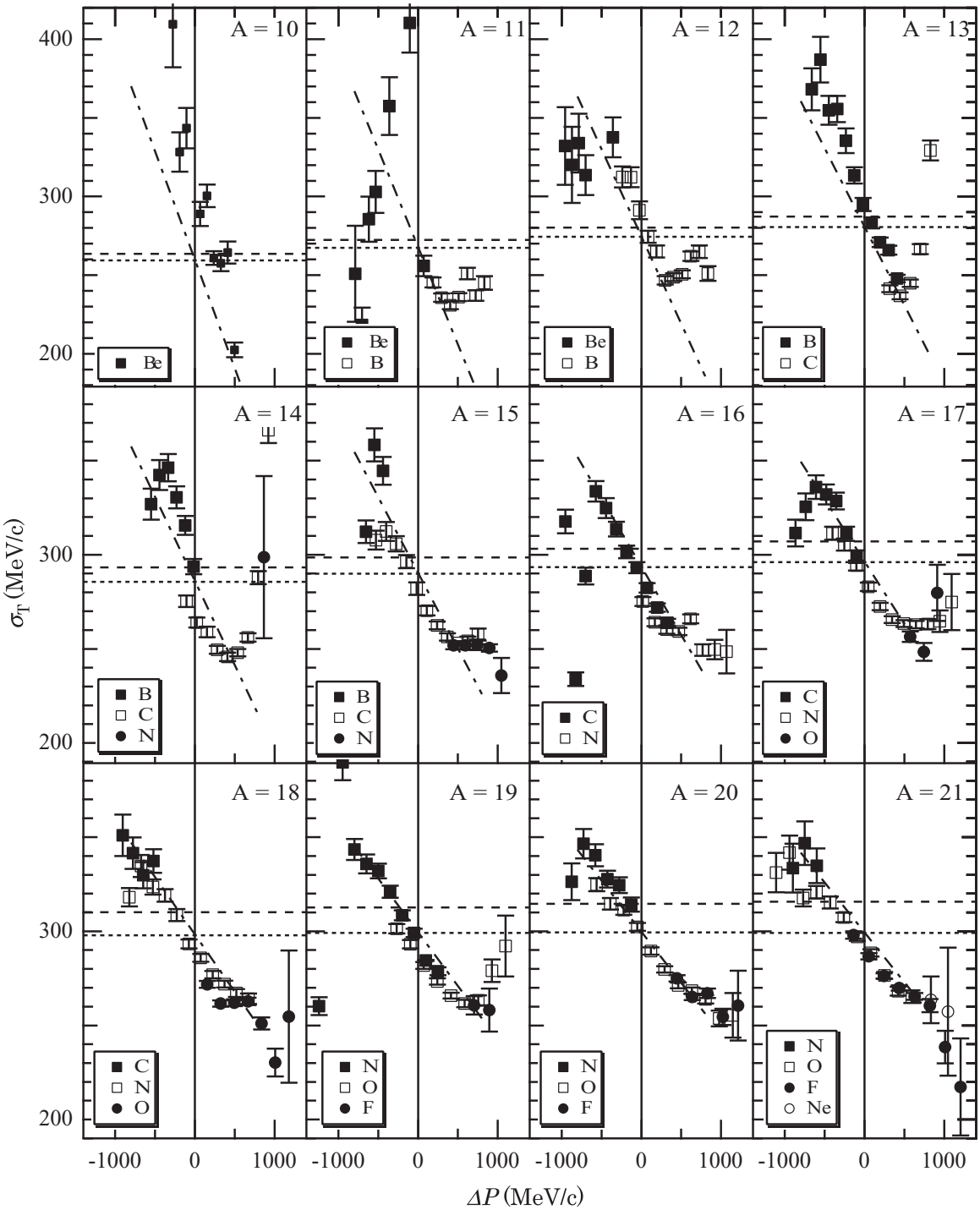

FIG. 4. Correlation between observed widths of P_T distributions and ΔP for fragments with A_F values of 10–21. The dotted and broken lines are as described in Fig. 3(b). Dot-and-dashed lines represent results calculated using the present formulation.

screen placed at the target position. The angular distributions of a wide range of fragments were observed by changing the rigidity of RIPS between $B\rho = 3.24$ and 3.96 Tm.

The fragments were identified event by event through measurements of time-of-flight (TOF) and energy loss (ΔE). A 1-mm-thick plastic scintillation counter (PL) and two 0.35-mm-thick silicon counters (Si) were installed at F2. The TOF of the fragment between the Be target and the F2 was determined from the difference in timing signal between the rf signal of the cyclotron and the PL timing. The ΔE of the fragment was measured by combining the two Si counters. The mass number A and atomic number Z of the fragments produced were obtained from the observed TOF, ΔE, and magnetic rigidity of RIPS $B\rho$. According to the charge-state distribution of fragments determined by the CHARGE code [16], the contributions of fragments, which were not fully stripped,

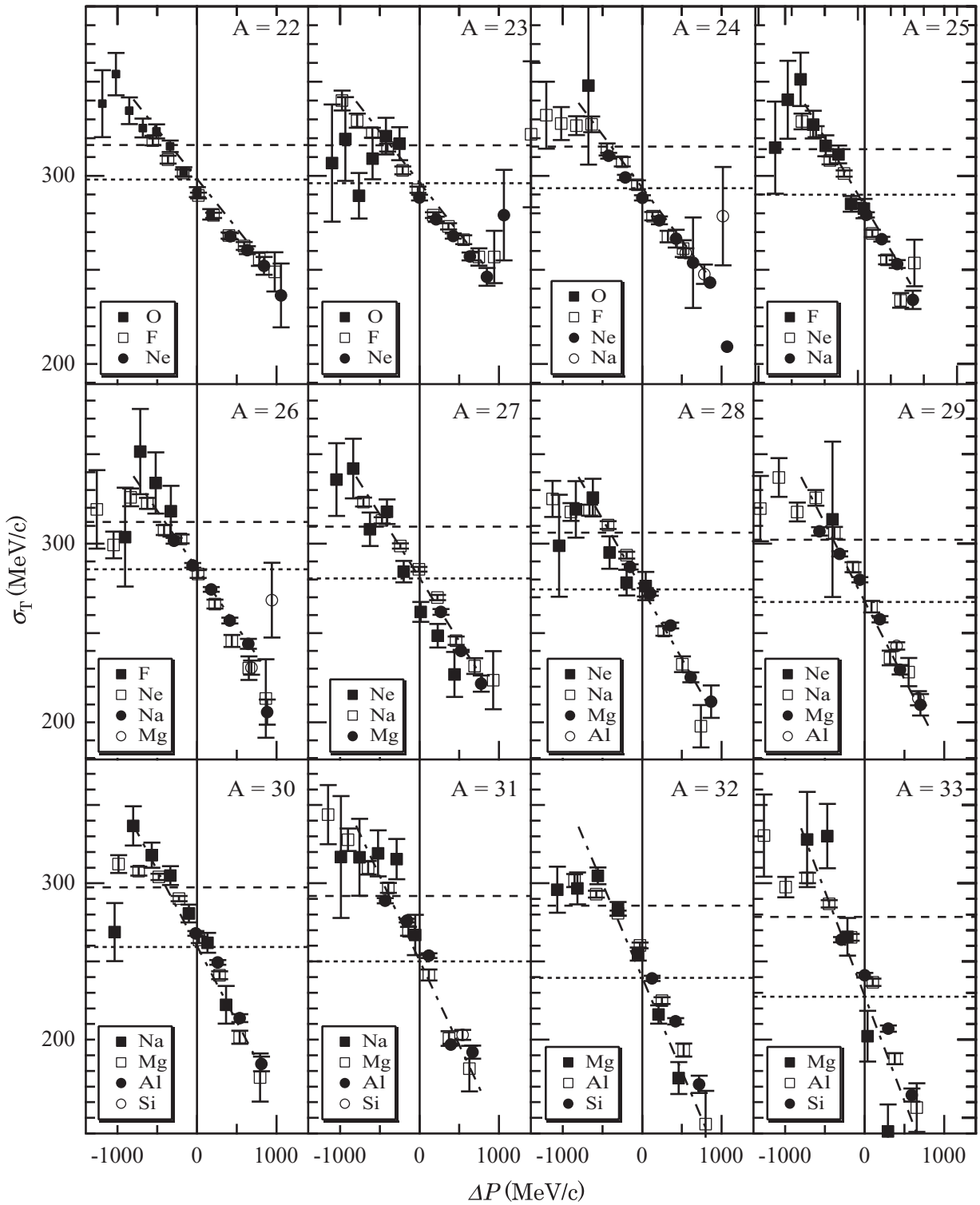

FIG. 5. Correlation between observed widths of P_T distributions and ΔP for fragments with A_F values of 22–33. Lines are as described in Fig. 4.

were less than 0.1% at 90 MeV/nucleon. Fragment yields were obtained by counting the isotopes identified by the above particle identification method.

The primary beam intensity was monitored for normalization of the fragment yields to obtain the angular distribution of production rates. The beam intensity was measured by a plastic telescope consisting of three plastic scintillators, placed at a backward position of the Be target. The telescope counter was capable of measuring the counting rate of charged particles scattered from the Be target. The counting rate of the

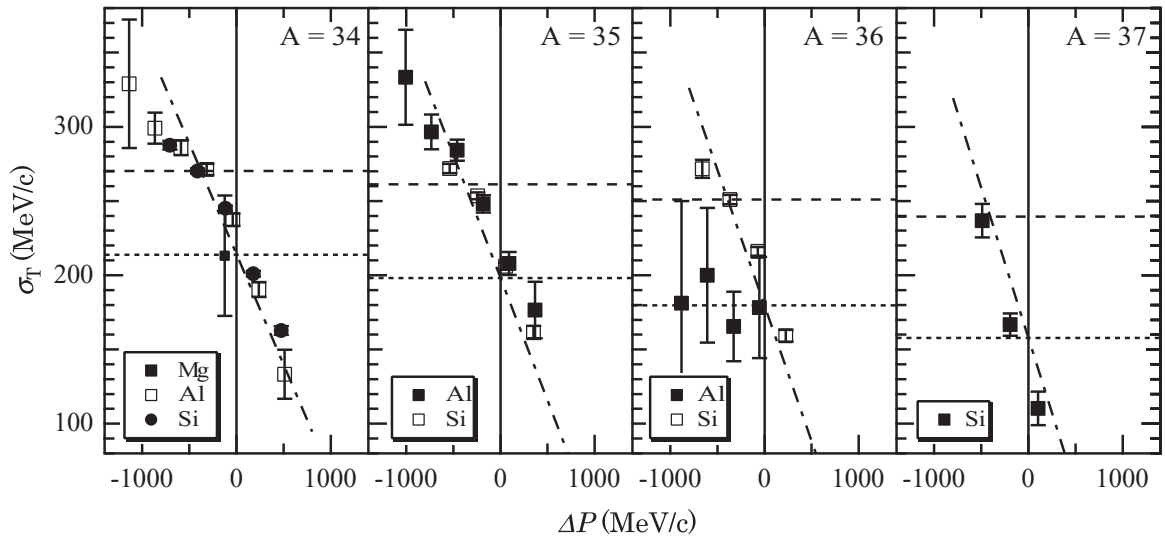

FIG. 6. Correlation between observed widths of P_T distributions and ΔP for fragments with A_F values of 34–37. Lines are as described in Fig. 4.

telescope counter was calibrated by a Faraday cup by changing the primary beam intensity. The relative error in the primary beam intensity arising from the uncertainty in the calibration was about ±5%. The swinger magnets allowed the orbit of fragments for counting after the Be target to keep the optical axis of the RIPS separator at any angle setting. Since four slits to define the angular acceptance of the RIPS separator were fixed, the solid angle acceptance could keep constant irrespective of the deflection angle. No detectors or degraders were installed between the Be target and the F2. Thus, it was concluded that the transmission value between the Be target and the F2 was estimated to be close to 100% for all deflection angles.

III. RESULTS AND DISCUSSION

The angular distributions of fragments observed at $B\rho$ = 3.60 Tm are shown in Fig. 1. The statistical error associated with counting the produced fragment and that associated with the primary beam intensity are considered to calculate error bars of the measured production rate. As seen in Fig. 1, the observed angular distribution shows a Gaussian-like distribution for a wide fragment mass range. The evolution of the angular distribution of ^{26}Ne with fragment velocity, observed at $B\rho$ = 3.312–3.888 Tm, is shown in Fig. 2. The figure shows a narrowing angular distribution trend for larger $B\rho$. In order to obtain the width of angular distribution, the observed angular distribution was fitted with a Gaussian function by taking account of the finite angular acceptance

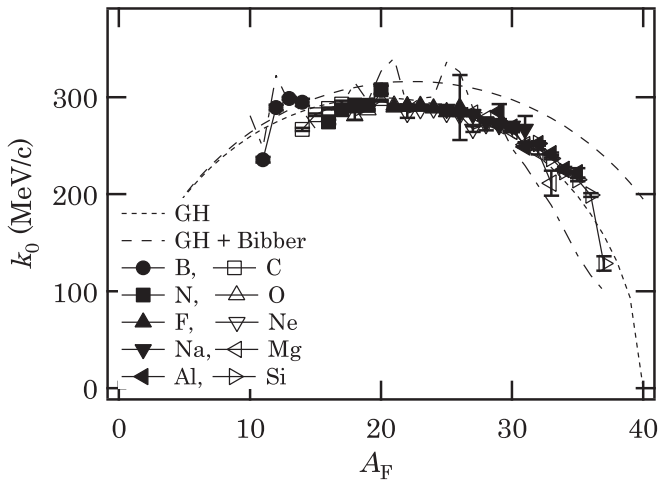

FIG. 7. Widths of P_T distribution at the projectile velocity as a function of A_F. The dotted line and broken line in the figure are as described in Fig. 3(b). The dot-and-dashed line represents the results of AMD calculation.

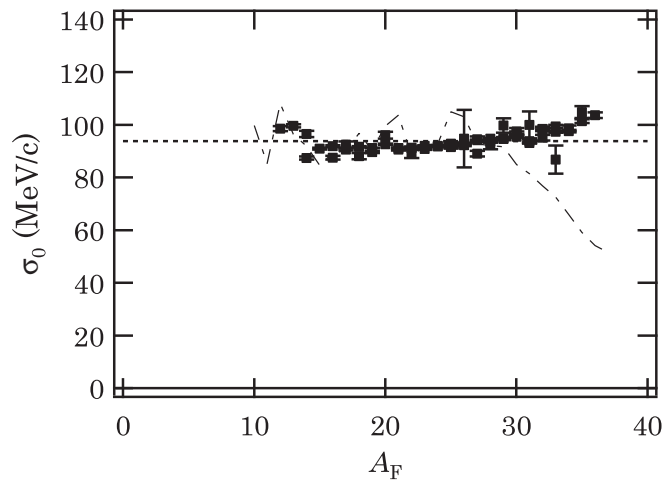

FIG. 8. Reduced width σ_0 calculated from k_0 according to the Goldhaber formula. The dotted line indicates the mean value of σ_0 = 93.6 MeV/c, obtained from the present results. The dot-and-dashed line indicates the results of the AMD calculation.

defined by the RIPS separator. The fits, indicated by the dotted lines in Fig. 1, well reproduce the observed angular distributions. The contribution of the angular straggling of fragments in the Be target as evaluated by ATIMA [14] was subtracted from the width obtained by the fit. The width of the P_T distribution σ_T was calculated from the obtained width of angular distribution, and P_L was determined by the rigidity of the RIPS separator. The P_L, evaluated for each fragment at the center position of the Be target, was used in the calculation.

As a typical example, Fig. 3 shows the correlation between σ_T, obtained by the above procedure, and the P_L for ^{26}Ne, with the P_L distribution observed at $\theta_x = 0$ mrad. σ_T shows a monotonic decreasing trend around the projectile velocity. The energy dissipation effect in reaction processes is observed as a shift in the P_L distribution from that corresponding to the projectile velocity, which is indicated by a vertical solid line in the figure. This shift in P_L, denoted by ΔP, is represented by the top axis in Fig. 3(a). The dotted line in Fig. 3(b) indicates the width σ_{GH}, which is calculated by the Goldhaber formula [4],

$$\sigma_{GH}^2 = \frac{A_F(A_P - A_F)}{A_P - 1}\sigma_0^2, \quad (1)$$

where A_P and A_F denote the mass numbers of the projectile and the fragment, respectively. The reduced width $\sigma_0 = 93.5\,\mathrm{MeV}/c$, obtained from the P_L distribution on the high-momentum side at $E_i = 90\,\mathrm{MeV/nucleon}$ [7], is used for the calculation. The broken line in Fig. 3(b) indicates the width σ_D, which incorporates the additional contribution of the orbital deflection of the projectile by the target [9] via

$$\sigma_D^2 = \sigma_{GH}^2 + \frac{A_F(A_F - 1)}{A_P(A_P - 1)}\sigma_1^2, \quad (2)$$

where σ_1 denotes the reduced width for the orbital deflection effect. $\sigma_1 = 195\,\mathrm{MeV}/c$ is used for calculation. σ_T agrees with σ_{GH}, rather than σ_D, at the projectile velocity, i.e., for $\Delta P = 0$. At higher velocities, i.e., for $\Delta P > 0$, σ_T is smaller than σ_{GH}. The relationship between the observed σ_T and the ΔP for fragments with mass numbers A_F between 10 and 37 is shown in Figs. 4–6. Those σ_T values having errors of less than $50\,\mathrm{MeV}/c$ are shown in the figure and employed in the following analysis. The σ_T values can be found in the Appendix. In Figs. 4–6, the monotonic decreasing trend of σ_T is clearly visible for all of the fragments, regardless of the isotope. For a few light fragments, the decreasing trend turns to an increasing trend at high momentum ($\Delta P > 500\,\mathrm{MeV}/c$).

TABLE I. The reduced width of the Goldhaber equation σ_0 and that of the orbital deflection effect σ_1, obtained from the observed P_T distributions. The reduced widths obtained from the observed P_L distributions [7], and those obtained from the P_T distributions [9,11] are included for reference.

Reaction	Energy (MeV/nucleon)	Reference	σ_0 (MeV/c)	σ_1 (MeV/c)
^{40}Ar + ^{9}Be	95	Present[a]	93.6 ± 1.3	0
^{40}Ar + ^{9}Be	95	Present[b]	93.6 (fixed)	213.6 ± 1.1
			97.9 ± 0.2 (free)	182.8 ± 2.1
^{40}Ar + ^{9}Be	90	[7]	93.5 ± 2.6	0
^{16}O + ^{27}Al	92.5	[9]	79.6 ± 2.1	223.5 ± 3.5
	117.5		88.1 ± 2.2	192.5 ± 4.4
^{76}Ge + ^{9}Be	130	[11]	86 ± 1	125 ± 1

[a]Obtained from σ_T at the projectile velocity.
[b]Obtained from σ_T at the center of the P_L distribution.

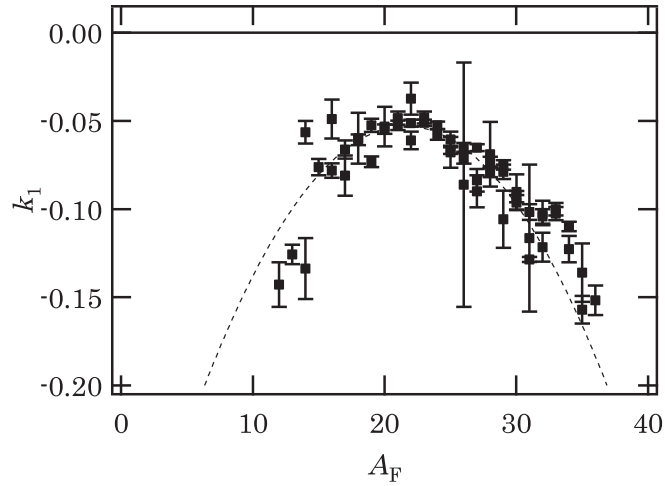

FIG. 9. The slope parameter obtained from σ_T. The dotted line indicates the results of fitting by a quadratic function.

In order to formulate the decreasing trend of σ_T, the σ_T values are analyzed by a linear function for each isotope. The linear function well reproduces the observed σ_T over the typical range $-800\,\mathrm{MeV}/c < \Delta P < +800\,\mathrm{MeV}/c$ as shown in Fig. 3(b). The width parameter k_0, σ_T at the projectile velocity, and the slope parameter k_1 are obtained from the curve fit. The σ_T behavior of Be isotopes differs from that of heavier isotopes (see Fig. 4), and the exchange reactions are dominant for ^{36}Al and ^{37}Si. Therefore, the fit was not applied to these fragments. The k_0 value obtained is in good agreement with the Goldhaber model [4] as seen in Fig. 7. The reduced width σ_0, which is calculated from k_0 via Eq. (1),

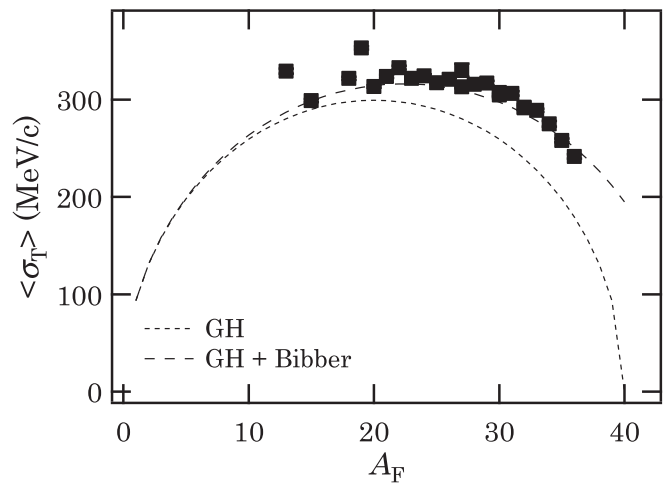

FIG. 10. Widths of P_T distributions at the center of the P_L distributions. The dotted line and broken line are as described in Fig. 3(b).

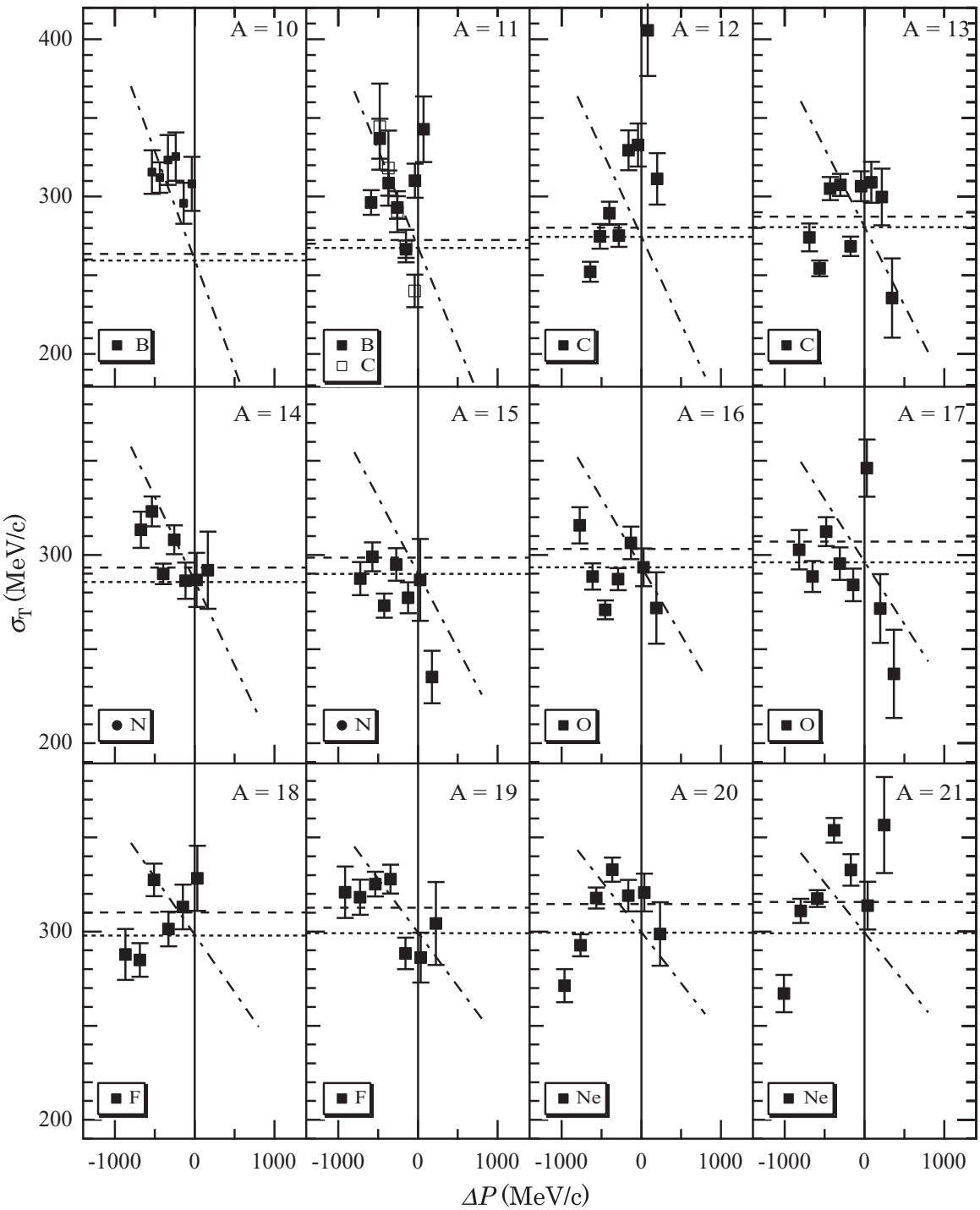

FIG. 11. Correlation between σ_T and ΔP as calculated by AMD for fragments with A_F values of 10–21. Lines are as described in Fig. 4.

is constant (see Fig. 8). The mean value of σ_0 for fragments with $A_F = 12$–36 is 93.6 ± 1.3 MeV/c. As seen in Table I, this value agrees well with that obtained from the P_L distribution in Ref. [7]. The slope parameter k_1 is plotted as a function of A_F in Fig. 9. Since k_1 shows a parabolic structure, it is fitted with a quadratic function. The dotted line in the figure represents the fit,

$$k_1 = -0.348 + 0.027\,3A_F - 0.000\,631A_F^2. \qquad (3)$$

The dot-and-dashed lines in Figs. 4–6, which are obtained from the above equation, well reproduce the observed results.

In most previous experimental and theoretical studies on the P_T distributions of fragments at incident energies of $\sim$100 MeV/nucleon, σ_T has been treated as a constant at all fragment velocities. The formulation in Ref. [9] was obtained on the basis of this framework. In order to compare our results with previous results, the most probable value of σ_T, $\langle\sigma_T\rangle$, is calculated. $\langle\sigma_T\rangle$ is σ_T at the center of the P_L distribution and

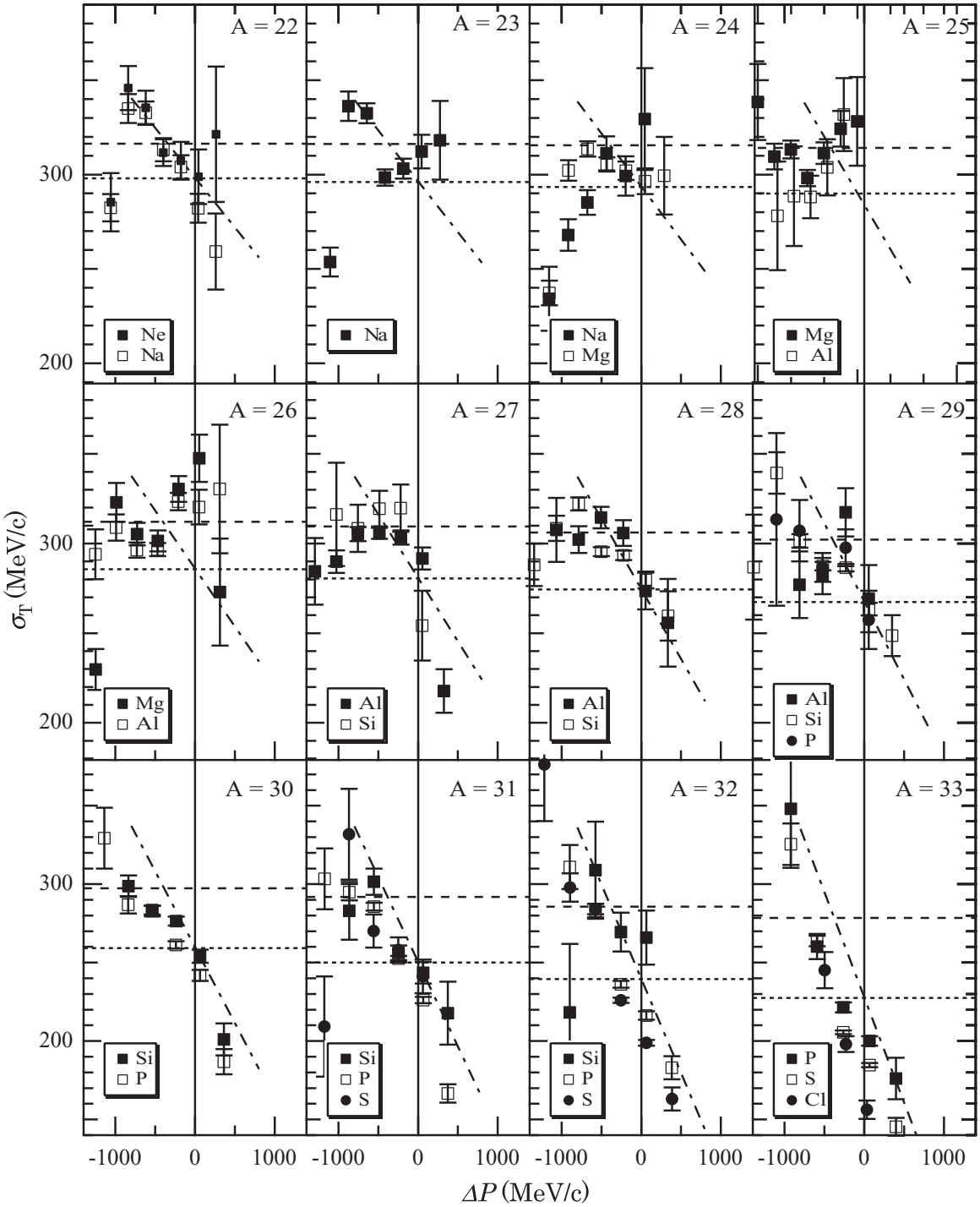

FIG. 12. Correlation between σ_T and ΔP as calculated by AMD for fragments with A_F values of 22–33. Lines are as described in Fig. 4.

is defined as

$$\langle \sigma_T \rangle = k_0 + k_1 \Delta P_0, \quad (4)$$

where ΔP_0 is the center of the P_L distribution relative to that corresponding to the projectile velocity. The calculation of ΔP_0 is based on the kinetic-energy loss ΔE, formulated in Ref. [7]. As shown in Fig. 10, the $\langle \sigma_T \rangle$ obtained is consistently larger than that predicted by the Goldhaber model and agrees with the formulation in Ref. [9]. The reduced width of the Goldhaber model σ_0 and that of the orbital deflection effect σ_1 were obtained from $\langle \sigma_T \rangle$ and shown in Table I. The σ_1 obtained is larger than that obtained in Ref. [11] and is comparable to the 195 MeV/c reported in Ref. [9].

The present systematical investigation of the P_T distribution revealed the behavior of their widths. In order to investigate such behavior, AMD calculations are performed for the reaction of $^{40}Ar + ^{9}Be$ subjected to an incident energy of 87.4 MeV/nucleon, which is slightly lower than in the present

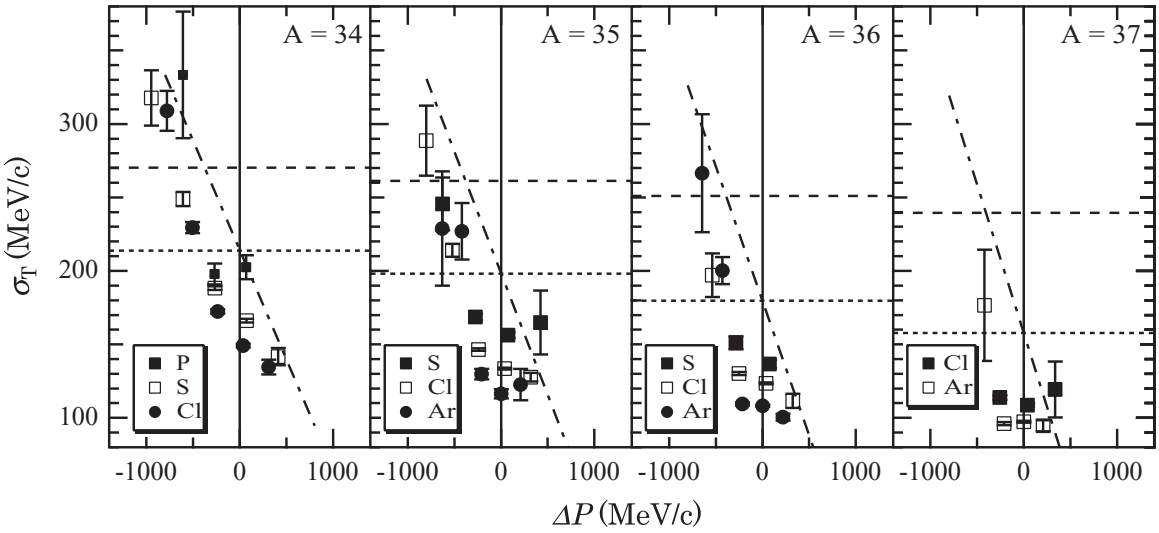

FIG. 13. Correlation between σ_T and ΔP as calculated by AMD for fragments with A_F values of 34–37. Lines are as described in Fig. 4.

experiment. Events were generated at impact parameter (b) values in the 0–12-fm range by AMD [17] with an effective interaction of the Gogny type. The decays of primary fragments, which were recognized at $t = 300\,\mathrm{fm}/c$, were calculated by a statistical decay code [18] to obtain the final products. P_T distributions, obtained through AMD calculations, are fitted by a Gaussian function to obtain σ_T. To maximize statistical precision, the fit is performed for fragments located close to the line of β stability. The correlation between σ_T and P_L is shown in Figs. 11–13. Those σ_T values with errors smaller than $50\,\mathrm{MeV}/c$ are shown in the figure. The σ_T obtained from the AMD calculation roughly reproduces the Goldhaber formulation results at the projectile velocity and decreasing trend as revealed in Figs. 4–6. The σ_T fit obtained through AMD calculation using a linear function is performed over the ΔP range from -800 to roughly $+800\,\mathrm{MeV}/c$ as in the case of the measured results. The fit is performed for each A_F without resolving isobars. For fragments with $A_F = 10$–30, the σ_T values at the projectile velocity k_0 and reduced width σ_0 obtained through AMD calculation follow the Goldhaber formulation and are consistent with the measured results as shown in Figs. 7 and 8. In contrast, AMD calculations consistently underestimate the widths for heavier fragments. In terms of the slope parameter, negative values, which correspond to a decreasing σ_T trend, are observed in Fig. 14. However, the large scatter and error associated with k_1 prevents further consideration of the contribution of A_F.

In Ref. [9], the contribution of a wide range of impact parameters is considered to be the cause of the additional width of the P_T distribution. In order to reveal the contribution of impact parameters, the P_T and P_L distributions are examined for ^{30}Si. Figure 15 shows a wide range of impact parameters contributing to the production of ^{30}Si. The productivity shows a maximum at an impact parameter b of around 5 to 6 fm. Figures 16 and 17 show the P_T and P_L distributions for each range of the impact parameter. In the case of a small impact

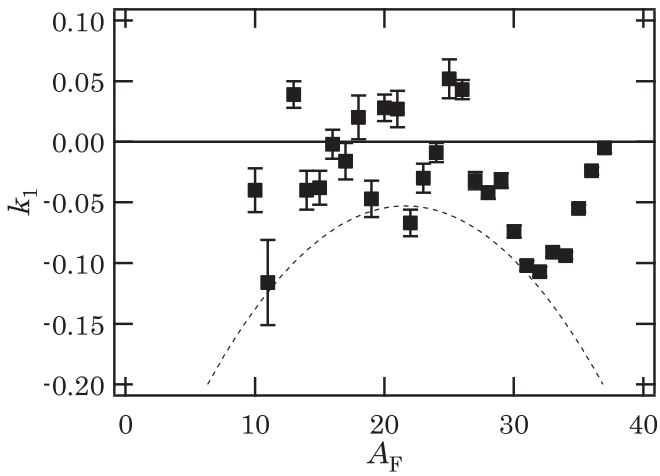

FIG. 14. Slope parameter obtained by AMD calculation. The dotted line is as in Fig. 9.

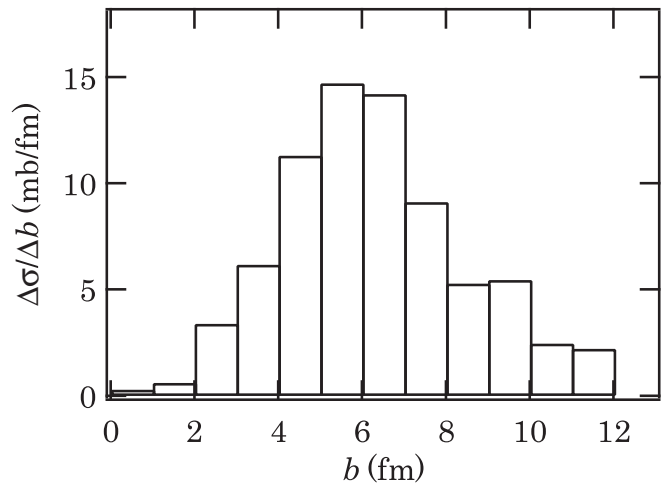

FIG. 15. Contribution of impact parameter to production cross section of ^{30}Si as obtained by AMD calculation.

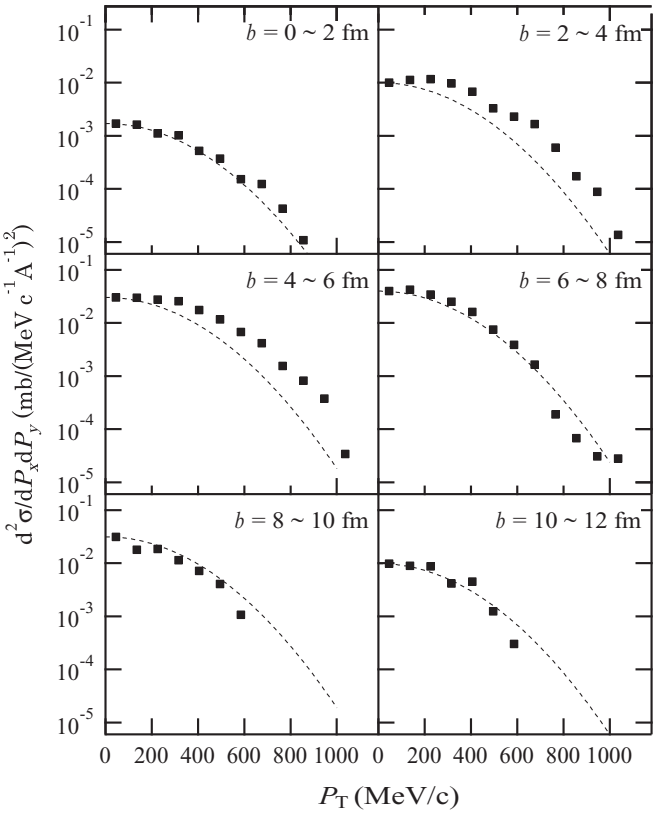

FIG. 16. P_T distributions of ^{30}Si obtained from AMD calculation. The ranges of the impact parameter are indicated in the figure. Dotted lines indicate Gaussian distributions with a width of 259.6 MeV/c as calculated by the Goldhaber equation. The amplitude is adjusted at the forward angle.

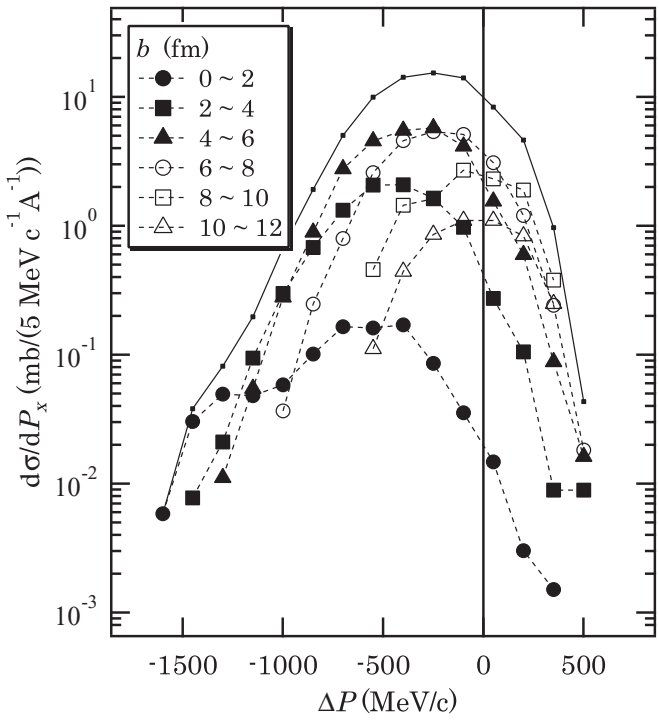

FIG. 17. P_L distributions of ^{30}Si obtained from AMD calculation. The ranges of the impact parameter are indicated in the legend. The solid line represents the sum of all ranges.

parameter ($0 < b < 6$ fm), σ_T is larger than that obtained by the Goldhaber formulation, and a relatively large energy dissipation effect is observed in the P_L distribution. By contrast, in the case of a larger impact parameter (6 fm $< b <$ 12 fm), σ_T is equal to or smaller than that obtained by the Goldhaber formulation, and the energy dissipation effect is relatively small. Thus, it is concluded that the observed decreasing σ_T trend is attributable to the evolution of the fragmentation process with respect to the impact parameter. In particular, the remarkably small σ_T observed at higher momentum is ascribed to the contribution of a large impact parameter.

IV. CONCLUSIONS

The angular distributions of fragments were investigated as a function of fragment velocity for a wide range of fragment masses produced by an Ar beam and Be target at 95 MeV/nucleon. The width of the P_T distribution σ_T, obtained from the measured angular distribution, shows a monotonic decreasing trend as a function of fragment velocity. σ_T at the projectile velocity agrees with the Goldhaber formulation. The most probable value of σ_T, defined at the center of the P_L distribution, is consistent with previous results in which σ_T was treated as a constant with respect to fragment velocity. It was confirmed that AMD calculation yields reliable results that can help to understand the observed P_T distribution. In particular, the correlation between P_L and σ_T was successfully explained on the basis of the evolution of the fragmentation process with respect to the impact parameter.

The present study is the first attempt to reveal the fragment velocity dependence of the P_T distribution during the fragmentation process at $E \approx 100$ MeV/nucleon. The observed σ_T and its variation with fragment velocity could be represented by a simple equation. This formulation is useful to obtain more reliable estimation of intensity and quality of radioactive nuclear beam, which is produced through the fragmentation process at this energy region.

ACKNOWLEDGMENT

The authors wish to thank the RIKEN Ring Cyclotron staff and crew for all of their support and for providing a high-quality Ar beam.

APPENDIX

This appendix tabulates the width of the observed P_T distribution for each fragment as a function of ΔP in Table II.

TABLE II. Width of P_T distributions σ_T of fragments as a function of ΔP. ΔP and σ_T are both in units of MeV/c.

	ΔP	σ_T		ΔP	σ_T		ΔP	σ_T
^{10}Be	−278.0	409.6 ± 27.3	^{14}B	−552.4	326.9 ± 8.2		−521.2	337.4 ± 6.3
	−192.4	328.2 ± 12.4		−445.6	342.3 ± 7.9	^{14}N	863.6	298.7 ± 43.1
	−106.6	343.5 ± 12.8		−338.5	346.3 ± 7.3	^{15}N	443.3	251.8 ± 2.0
	−20.8	455.3 ± 30.2		−231.4	330.6 ± 5.9		593.0	251.9 ± 2.2
	65.1	288.9 ± 7.7		−124.3	315.6 ± 5.0		742.8	252.1 ± 2.8
	150.9	300.4 ± 7.2		−17.1	293.7 ± 4.0		892.5	250.4 ± 2.0
	236.8	260.8 ± 4.3	^{15}B	−656.3	312.3 ± 6.0		1042.7	235.9 ± 9.3
	322.8	257.5 ± 5.0		−549.4	358.4 ± 8.8	^{16}N	19.7	275.1 ± 2.4
	408.7	264.4 ± 7.0		−442.2	344.6 ± 7.5		169.2	264.2 ± 2.1
	494.7	202.5 ± 4.7	^{13}C	314.7	241.3 ± 2.2		318.7	260.3 ± 2.2
^{11}Be	−789.5	250.8 ± 30.6		443.2	236.9 ± 2.1		468.4	259.2 ± 1.9
	−703.9	218.4 ± 11.0		571.7	245.0 ± 2.3		618.2	265.9 ± 2.3
	−618.4	285.5 ± 14.4		697.3	266.6 ± 3.1		768.0	249.4 ± 3.1
	−532.8	303.0 ± 13.3		826.1	329.2 ± 6.4		918.0	249.7 ± 5.2
	−361.5	357.5 ± 18.4		955.0	423.4 ± 14.1		1068.0	248.6 ± 11.5
	−275.7	521.6 ± 43.5	^{14}C	−106.9	275.3 ± 3.1	^{17}N	−401.9	311.4 ± 3.5
	−189.9	466.7 ± 25.9		21.3	264.1 ± 2.7		−252.8	305.5 ± 3.2
	−104.2	410.3 ± 18.8		149.7	259.0 ± 2.8		−103.5	294.3 ± 2.6
	−18.3	511.2 ± 38.3		278.1	249.5 ± 2.0		46.0	283.0 ± 2.2
	67.6	255.9 ± 6.5		406.5	245.8 ± 2.3		195.6	272.5 ± 1.9
^{12}Be	−957.3	332.0 ± 24.6		535.1	248.0 ± 2.0		345.2	265.6 ± 1.8
	−871.9	320.1 ± 24.2		663.8	256.0 ± 2.2		495.0	263.5 ± 1.8
	−786.3	333.9 ± 18.7		792.5	287.8 ± 3.5		644.8	262.8 ± 1.9
	−700.8	313.6 ± 12.7		921.2	366.2 ± 6.8		794.8	263.2 ± 2.6
	−615.1	457.4 ± 28.5	^{15}C	−531.2	307.8 ± 5.1		944.8	264.7 ± 5.8
	−529.5	420.2 ± 22.4		−403.2	312.3 ± 5.1		1094.9	274.9 ± 15.0
	−357.9	337.5 ± 12.7		−275.1	305.7 ± 4.1	^{18}N	−824.5	318.1 ± 4.8
^{11}B	186.0	245.3 ± 3.1		−146.9	296.3 ± 3.4		−675.6	334.7 ± 5.8
	293.2	235.7 ± 2.7		−18.6	281.9 ± 3.4		−526.5	323.5 ± 4.0
	400.4	245.3 ± 3.1		109.8	270.2 ± 2.4		−377.4	319.0 ± 3.4
	507.7	236.0 ± 2.5		238.3	262.5 ± 2.2		−228.1	308.7 ± 3.2
	615.0	251.0 ± 3.7		366.8	256.3 ± 2.0		−78.6	293.3 ± 2.4
	722.3	237.1 ± 3.4		495.4	253.2 ± 0.3		70.9	285.9 ± 2.1
	829.7	245.1 ± 4.3		624.0	254.3 ± 2.3		220.6	276.9 ± 1.9
^{12}B	−238.4	312.5 ± 6.6		752.7	257.6 ± 3.1		370.4	272.0 ± 1.8
	−131.4	312.2 ± 6.4	^{16}C	−953.6	317.6 ± 6.2		519.4	267.2 ± 2.1
	−24.3	291.3 ± 5.6		−825.8	233.9 ± 3.7		670.1	264.1 ± 2.8
	82.8	274.5 ± 3.8		−698.1	288.7 ± 4.5	^{19}N	−1245.3	260.3 ± 4.7
	189.9	265.0 ± 3.9		−570.1	333.7 ± 5.4		−948.1	389.8 ± 9.4
	297.2	246.8 ± 2.6		−442.0	324.8 ± 5.4		−799.1	343.5 ± 5.6
	404.4	248.7 ± 2.5		−313.9	313.6 ± 4.0		−650.2	335.7 ± 5.0
	511.7	250.5 ± 2.5		−185.6	301.5 ± 3.4		−500.9	332.0 ± 4.0
	619.1	262.1 ± 3.0		−57.2	293.2 ± 2.9		−351.7	321.0 ± 3.2
	726.5	264.8 ± 4.0		71.2	282.4 ± 2.5		−202.2	308.5 ± 2.6
	833.8	251.1 ± 4.6		199.7	272.0 ± 2.2		−52.6	299.1 ± 2.3
^{13}B	−661.5	368.1 ± 13.4		328.3	263.8 ± 2.1		97.0	284.4 ± 0.3
	−554.7	386.9 ± 14.5	^{17}C	−866.5	311.6 ± 7.1		246.8	278.8 ± 2.1
	−447.9	354.9 ± 9.2		−738.6	325.5 ± 7.1	^{20}N	−874.9	326.3 ± 9.8
	−341.0	355.7 ± 8.3		−610.6	335.9 ± 6.3		−725.7	346.5 ± 7.8
	−234.0	335.4 ± 7.9		−482.4	332.1 ± 5.2		−576.6	340.3 ± 5.9
	−127.0	313.5 ± 5.2		−355.2	328.6 ± 4.5		−427.2	327.6 ± 4.4
	−19.8	294.9 ± 4.2		−225.8	311.1 ± 3.8		−277.7	324.5 ± 4.2
	87.3	283.3 ± 3.5		−97.5	299.0 ± 3.3		−128.2	314.2 ± 3.7
	194.5	270.8 ± 3.0	^{18}C	−905.7	350.9 ± 11.0	^{21}N	−1048.3	400.6 ± 29.1
	301.8	265.9 ± 2.8		−777.6	341.5 ± 8.3		−899.2	333.5 ± 13.0
	409.1	248.0 ± 2.4		−649.5	329.9 ± 7.0		−750.0	346.8 ± 11.5

TABLE II. (*Continued.*)

	ΔP	σ_T		ΔP	σ_T		ΔP	σ_T
	−600.6	334.8 ± 9.2		−252.7	317.1 ± 8.7	^{26}F	−905.4	303.7 ± 27.7
^{17}O	572.0	256.5 ± 2.7	^{24}O	−675.5	347.8 ± 42.0		−714.0	351.4 ± 23.9
	742.9	248.4 ± 4.8	^{19}F	701.6	260.7 ± 4.9		−522.6	334.0 ± 17.1
	914.0	279.7 ± 14.9		893.7	258.2 ± 11.4		−330.9	318.1 ± 14.2
^{18}O	151.5	271.8 ± 1.8	^{20}F	445.1	275.0 ± 1.7	^{21}Ne	833.8	263.6 ± 12.4
	322.0	261.6 ± 1.6		636.9	265.1 ± 1.7		1047.0	257.4 ± 34.0
	492.8	262.0 ± 1.8		828.9	267.1 ± 2.5	^{22}Ne	415.4	267.9 ± 1.7
	663.7	262.7 ± 2.0		1020.9	254.5 ± 4.3		628.6	260.5 ± 2.1
	834.8	251.0 ± 3.3		1213.2	260.5 ± 18.5		841.3	252.1 ± 4.7
	1006.0	230.3 ± 7.4	^{21}F	−138.7	298.0 ± 1.9		1054.5	236.5 ± 17.0
	1177.2	254.7 ± 35.1		52.8	286.7 ± 1.6	^{23}Ne	−4.9	288.3 ± 1.6
^{19}O	−270.5	301.4 ± 2.4		244.4	276.3 ± 1.4		207.6	276.8 ± 1.4
	−100.3	293.1 ± 2.2		436.2	269.9 ± 1.4		420.2	267.9 ± 1.4
	70.2	281.8 ± 1.8		628.2	265.4 ± 1.8		633.2	257.2 ± 2.1
	240.9	273.3 ± 1.6		820.3	260.6 ± 3.4		846.6	246.3 ± 4.8
	411.7	265.8 ± 1.6		1012.7	238.5 ± 8.6		1059.7	279.1 ± 24.1
	582.6	261.6 ± 2.0		1205.1	217.3 ± 25.8	^{24}Ne	−423.1	310.6 ± 1.9
	753.7	263.3 ± 2.7	^{22}F	−559.0	318.8 ± 2.6		−211.0	299.1 ± 1.6
	924.8	279.1 ± 5.9		−367.9	308.5 ± 2.1		1.4	288.2 ± 1.4
	1096.1	292.2 ± 16.2		−176.7	301.4 ± 1.8		214.0	276.4 ± 1.3
^{20}O	−561.3	324.7 ± 3.6		14.9	289.5 ± 1.6		426.7	266.6 ± 1.5
	−391.2	314.6 ± 3.0		206.6	278.9 ± 1.5		639.8	253.7 ± 2.7
	−221.1	311.3 ± 2.5		398.4	268.2 ± 1.6		853.1	243.3 ± 5.2
	−50.8	302.4 ± 2.1		590.5	262.7 ± 2.0		1066.5	209.2 ± 17.4
	119.8	289.5 ± 2.0		782.7	255.7 ± 3.6	^{25}Ne	−843.0	328.9 ± 4.2
	290.5	279.8 ± 1.7		975.0	248.9 ± 10.4		−631.2	323.4 ± 2.9
	461.2	271.3 ± 1.5	^{23}F	−977.9	339.9 ± 5.3		−419.3	308.1 ± 2.0
	632.2	268.4 ± 1.7		−787.2	329.3 ± 3.8		−207.1	301.2 ± 1.7
	803.3	263.9 ± 2.2		−596.2	322.9 ± 2.7		5.5	284.1 ± 1.6
	974.5	253.6 ± 4.1		−405.1	315.0 ± 2.1		218.3	269.3 ± 1.9
	1145.7	255.3 ± 11.8		−213.7	302.9 ± 2.0		431.1	255.3 ± 2.3
^{21}O	−1111.3	331.1 ± 10.5		−22.1	292.5 ± 1.7		644.3	233.7 ± 3.9
	−941.9	341.8 ± 9.0		169.7	279.2 ± 1.5		857.6	253.7 ± 12.3
	−771.9	317.6 ± 4.4		361.6	273.1 ± 1.7	^{26}Ne	−1261.7	319.2 ± 22.0
	−601.8	320.8 ± 3.3		553.7	266.1 ± 2.3		−1050.3	299.2 ± 7.5
	−431.7	315.2 ± 3.2		746.0	256.9 ± 4.6		−839.0	325.9 ± 4.9
	−261.2	307.4 ± 2.6		938.3	256.9 ± 13.8		−627.0	322.5 ± 3.1
	−90.6	297.1 ± 2.1	^{24}F	−1398.0	322.0 ± 38.8		−414.8	305.8 ± 2.4
	80.0	288.5 ± 1.9		−1207.5	332.2 ± 17.8		−202.5	302.7 ± 2.5
	250.9	276.5 ± 1.8		−1017.0	327.7 ± 8.7		10.2	283.0 ± 2.1
	421.8	268.2 ± 2.3		−826.2	326.6 ± 5.0		223.1	266.3 ± 2.5
	592.9	265.3 ± 3.4		−635.1	327.3 ± 4.2		436.0	245.6 ± 3.4
^{22}O	−1191.8	337.9 ± 17.8		−444.0	314.0 ± 3.2		649.4	230.4 ± 6.5
	−1022.2	353.6 ± 11.2		−252.4	307.5 ± 2.5		862.8	213.4 ± 22.0
	−852.2	334.1 ± 7.0		−60.7	295.2 ± 2.3	^{27}Ne	−1470.8	181.5 ± 32.0
	−682.2	325.0 ± 5.0		131.1	278.6 ± 2.2		−1048.2	335.8 ± 20.3
	−511.8	323.2 ± 3.8		323.1	267.6 ± 3.1		−836.7	342.0 ± 16.6
	−341.3	315.3 ± 3.1		515.3	261.3 ± 4.5		−624.5	308.0 ± 9.4
	−170.8	301.6 ± 2.5	^{25}F	−1246.6	314.9 ± 24.5		−412.1	317.8 ± 6.9
	0.0	290.9 ± 2.7		−1056.0	340.4 ± 20.8		−199.7	284.3 ± 6.0
	170.9	279.0 ± 2.8		−865.0	351.2 ± 14.1		13.2	261.8 ± 5.6
^{23}O	−1104.4	306.8 ± 31.2		−673.8	327.2 ± 7.4		226.2	248.6 ± 6.6
	−934.3	319.6 ± 22.3		−482.6	316.0 ± 5.5		439.2	226.8 ± 12.6
	−764.2	289.4 ± 12.0		−290.9	311.3 ± 4.7	^{28}Ne	−1045.0	298.9 ± 28.5
	−593.8	309.2 ± 11.0		−99.1	285.0 ± 4.2		−833.1	319.1 ± 15.8
	−423.4	321.1 ± 9.7		92.7	282.6 ± 5.1		−620.9	325.7 ± 10.6

TABLE II. (*Continued.*)

	ΔP	σ_T		ΔP	σ_T		ΔP	σ_T
	−408.3	295.0 ± 9.0	^{26}Mg	683.9	230.6 ± 3.9		390.9	196.8 ± 0.4
	−195.8	278.2 ± 7.1		938.7	268.4 ± 20.9		666.6	192.0 ± 4.2
	43.0	276.2 ± 7.9	^{27}Mg	265.3	261.8 ± 1.6	^{32}Al	−851.3	301.8 ± 4.2
^{29}Ne	−405.8	313.5 ± 43.4		519.6	240.0 ± 0.7		−577.7	293.1 ± 2.1
^{24}Na	547.5	258.9 ± 2.6		774.3	221.7 ± 4.6		−303.2	280.8 ± 1.7
	781.4	247.6 ± 5.1		1029.5	59.8 ± 18.4		−28.3	260.3 ± 1.8
	1015.5	278.5 ± 26.1	^{28}Mg	−152.2	286.9 ± 1.4		246.8	225.0 ± 2.3
^{25}Na	129.3	279.2 ± 1.4		101.9	272.1 ± 1.1		522.3	193.3 ± 4.1
	362.9	266.4 ± 1.3		356.3	254.2 ± 1.6		798.3	146.0 ± 21.2
	596.7	253.1 ± 2.0		611.0	225.2 ± 2.8	^{33}Al	−1267.9	330.5 ± 26.3
	830.7	234.0 ± 4.9		866.0	211.6 ± 9.1		−994.9	297.6 ± 6.5
	1065.0	171.5 ± 19.4	^{29}Mg	−571.2	306.9 ± 2.3		−720.9	303.4 ± 3.3
^{26}Na	−289.7	301.7 ± 1.6		−317.5	294.3 ± 1.5		−446.4	286.9 ± 2.4
	−56.6	287.8 ± 1.3		−63.5	279.8 ± 1.4		−171.9	265.5 ± 2.2
	176.7	274.4 ± 1.2		190.6	257.7 ± 1.8		103.4	236.7 ± 2.4
	410.4	257.0 ± 1.6		445.3	229.5 ± 2.7		379.0	187.8 ± 3.6
	644.4	243.9 ± 2.8		700.3	209.8 ± 5.9		654.9	156.5 ± 15.6
	878.6	205.8 ± 7.0		955.5	174.9 ± 48.2	^{34}Al	−1139.7	328.9 ± 43.2
^{27}Na	−707.8	323.3 ± 2.5	^{30}Mg	−988.5	312.3 ± 5.6		−865.6	299.0 ± 10.5
	−475.4	313.0 ± 1.8		−735.3	307.7 ± 2.8		−591.5	286.0 ± 5.0
	−242.4	298.6 ± 1.4		−481.9	304.1 ± 2.0		−316.7	271.3 ± 3.8
	−9.0	285.6 ± 1.3		−228.1	290.3 ± 1.7		−41.4	237.4 ± 4.1
	224.6	269.9 ± 1.5		26.2	263.7 ± 1.9		233.9	190.3 ± 4.9
	458.3	245.7 ± 2.3		280.9	241.1 ± 2.5		509.8	133.3 ± 16.4
	692.5	231.5 ± 4.5		535.6	201.6 ± 4.3	^{35}Al	−1009.4	333.4 ± 32.0
	926.8	223.6 ± 16.2		790.8	175.7 ± 15.3		−735.2	296.6 ± 11.7
^{28}Na	−1126.8	325.1 ± 10.1	^{31}Mg	−1154.4	343.8 ± 18.9		−460.3	284.3 ± 7.0
	−895.0	317.7 ± 5.0		−901.5	327.9 ± 7.2		−185.4	248.1 ± 5.9
	−662.2	318.8 ± 3.1		−648.1	309.9 ± 4.3		90.2	208.0 ± 7.7
	−429.3	310.4 ± 2.2		−394.2	297.0 ± 3.3		366.1	176.6 ± 19.1
	−196.3	293.6 ± 1.9		−140.1	269.2 ± 2.8	^{36}Al	−605.6	199.9 ± 45.4
	37.3	272.7 ± 2.3		114.4	241.4 ± 3.4		−328.9	165.5 ± 23.4
	271.2	251.1 ± 2.6		369.3	200.8 ± 4.7		−54.9	178.3 ± 34.2
	505.0	232.6 ± 4.3		624.4	181.5 ± 14.5	^{30}Si	956.5	135.0 ± 25.7
	739.3	197.8 ± 11.8	^{32}Mg	−1066.3	295.9 ± 14.7	^{31}Si	538.8	203.0 ± 3.1
^{29}Na	−1313.7	319.6 ± 18.3		−812.8	296.8 ± 10.1	^{32}Si	122.9	239.1 ± 1.6
	−1081.4	337.1 ± 10.9		−559.2	304.7 ± 5.4		418.8	211.7 ± 2.1
	−849.0	317.7 ± 5.3		−305.0	283.6 ± 4.3		715.0	171.5 ± 5.5
	−616.2	325.6 ± 4.5		−50.4	254.8 ± 4.2	^{33}Si	−294.7	263.9 ± 1.7
	−383.0	306.1 ± 3.3		204.1	216.2 ± 5.9		0.7	241.2 ± 1.6
	−149.7	286.8 ± 2.8		459.2	175.4 ± 10.1		296.3	207.1 ± 2.0
	84.0	264.7 ± 3.2	^{33}Mg	−725.6	328.0 ± 30.4		592.4	164.6 ± 4.2
	318.0	236.0 ± 4.1		−471.4	330.2 ± 20.6	^{34}Si	−710.4	287.6 ± 2.9
	552.2	228.2 ± 7.8		−217.2	265.8 ± 12.1		−415.6	270.2 ± 1.8
	786.5	157.9 ± 26.0		37.6	202.1 ± 16.2		−120.5	245.1 ± 1.7
^{30}Na	−1036.7	268.7 ± 18.5		292.6	141.3 ± 17.2		175.1	201.0 ± 1.9
	−803.8	336.6 ± 12.5	^{34}Mg	−128.1	213.3 ± 40.6		471.4	162.8 ± 2.9
	−571.0	318.0 ± 8.0	^{28}Al	818.0	178.7 ± 14.5	^{35}Si	−539.1	271.9 ± 3.1
	−337.5	304.9 ± 6.0	^{29}Al	401.3	242.7 ± 2.0		−244.1	253.5 ± 2.4
	−103.8	280.6 ± 5.7		676.7	213.6 ± 4.0		51.8	206.1 ± 2.3
	129.9	262.0 ± 6.4	^{30}Al	−16.7	267.9 ± 1.5		348.0	161.5 ± 4.5
	364.1	222.2 ± 12.0		258.2	249.4 ± 1.6	^{36}Si	−661.1	271.6 ± 6.1
^{31}Na	−991.3	316.8 ± 38.9		533.3	213.8 ± 2.5		−365.7	251.0 ± 3.2
	−758.1	316.6 ± 24.6		809.0	184.5 ± 4.7		−69.9	216.0 ± 2.9
	−524.9	319.0 ± 14.7	^{31}Al	−433.5	288.9 ± 1.6		226.0	159.3 ± 3.9
	−291.3	315.4 ± 12.8		−159.3	276.2 ± 1.2	^{37}Si	−489.3	236.8 ± 11.2
	−57.4	266.9 ± 12.8		115.5	253.8 ± 1.4		−193.8	166.8 ± 7.6
							102.4	110.2 ± 11.2

[1] O. B. Tarasov and D. Bazin, Nucl. Instrum. Methods Phys. Res., Sect. B **266**, 4657 (2008).
[2] N. Iwasa, H. Geissel, G. Münzenberg, C. Scheidenberger, T. Schwab, and H. Wollnik, Nucl. Instrum. Methods Phys. Res., Sect. B **126**, 284 (1997).
[3] D. E. Greiner, P. J. Lindstrom, H. H. Heckman, B. Cork, and F. S. Bieser, Phys. Rev. Lett. **35**, 152 (1975).
[4] A. S. Goldhaber, Phys. Lett. B **53**, 306 (1974).
[5] F. Rami, J. P. Coffin, G. Guillaume, B. Heusch, P. Wagner, A. Fahli, and P. Fintz, Nucl. Phys. A **444**, 325 (1985).
[6] V. Borrel, D. Guerreau, J. Galin, B. Gatty, D. Jacquet, and X. Tarrago, Z. Phys. A: At. Nucl. **314**, 191 (1983).
[7] M. Notani, H. Sakurai, N. Aoi, H. Iwasaki, N. Fukuda, Z. Liu, K. Yoneda, H. Ogawa, T. Teranishi, T. Nakamura, H. Okuno, A. Yoshida, Y. X. Watanabe, S. Momota, N. Inabe, T. Kubo, S. Ito, A. Ozawa, T. Suzuki, I. Tanihata, and M. Ishihara, Phys. Rev. C **76**, 044605 (2007).
[8] O. Tarasov, Nucl. Phys. A **734**, 536 (2004).
[9] K. Van Bibber, D. L. Hendrie, D. K. Scott, H. H. Weiman, L. S. Schroeder, J. V. Geaga, S. A. Cessin, R. Treuhaft, Y. J. Grossiord, J. O. Rasmussen, and C. Y. Wong, Phys. Rev. Lett. **43**, 840 (1979).
[10] J. M. Kidd, P. J. Lindstrom, H. J. Crawford, and G. Woods, Phys. Rev. C **37**, 2613 (1988).
[11] K. Meierbachtol, D. J. Morrissey, M. Mosby, and D. Bazin, Phys. Rev. C **85**, 034608 (2012).
[12] C. Y. Wong and K. Van Bibber, Phys. Rev. C **25**, 2990 (1982).
[13] S. Momota, I. Tanihata, A. Ozawa, M. Notani, K. Yoshida, K. Morimoto, T. Onishi, T. Yamaguchi, A. Yoshida, Y. X. Watanabe, L. Zhong, M. Kanazawa, A. Kitagawa, M. Suda, and Y. Nojiri, Nucl. Phys. A **746**, 407 (2004).
[14] H. Geissel, C. Scheidenberger, P. Malzacher, J. Kunzendorf, and H. Weick, computer code ATIMA, GSI, https://web-docs.gsi.de/∼weick/atima/.
[15] T. Kubo, M. Ishihara, N. Inabe, H. Kumagai, I. Tanihata, K. Yoshida, T. Nakamura, H. Okuno, S. Shimoura, and K. Asahi, Nucl. Instrum. Methods Phys. Res., Sect. B **70**, 309 (1992).
[16] C. Scheidenberger, T. Stöhlker, W. E. Meyerhof, H. Geissel, P. H. Mokler, and B. Blank, Nucl. Instrum. Methods Phys. Res., Sect. B **142**, 441 (1998).
[17] A. Ono, Phys. Rev. C **59**, 853 (1999).
[18] T. Maruyama, A. Ono, A. Ohnishi, and H. Horiuchi, Prog. Theor. Phys. **87**, 1367 (1992).